A Coupled Experiment with LICOM2 as the Ocean Component of CESM1

LIN Pengfei[1] (林鹏飞), LIU Hailong[1*] (刘海龙), XUE Wei[2] (薛 巍), LI Huimin[2] (李慧岷),

JIANG Jinrong[3] (姜金荣), SONG Mirong[1] (宋米荣), SONG Yi[1] (宋 毅),

WANG Fuchang[1] (王夫常), and ZHANG Minghua[4,5] (张明华)

1 *State Key Laboratory of Numerical Modeling for Atmospheric Sciences and Geophysical Fluid Dynamics, Institute of Atmospheric Physics, Chinese Academy of Sciences, Beijing* 100029, *China*

2 *Department of Computer Science and Technology, Tsinghua University, Beijing* 100084, *China*

3 *Computer Network Information Center, Chinese Academy of Sciences, Beijing* 100190, *China*

4 *Stony Brook University, Stony Brook, NY* 11794, *USA*

5 *International Center for Climate and Environment Sciences, Institute of Atmospheric Physics, Beijing* 100029, *China*

(Received May 20, 2015; in final form September 29, 2015)

ABSTRACT

In the present study, the LASG/IAP Climate system Ocean Model version 2 (LICOM2) was implemented to replace the original ocean component in the Community Earth System Model version 1.0.4 (CESM1) to form a new coupled model referred to as CESM1+LICOM2. The simulation results from a 300-yr preindustrial experiment by using this model were evaluated against both observations and the Flexible Global Ocean-Atmosphere-Land System Model with grid-atmospheric model version 2 (FGOALS-g2). It was found that CESM1+LICOM2 simulates well the mean features of the ocean, sea ice, and atmosphere, relative to models used in the Coupled Model Intercomparison Experiment (CMIP5), when compared with observations. The spatial distribution of SST bias in CESM1+LICOM2 is similar to that in the Community Climate System Model version 4 (CCSM4). The simulated climate variabilities, such as ENSO and Pacific decadal oscillation, are also reasonably simulated when compared with observations. The successful implementation of LICOM2 in the CESM1 framework greatly enhances the capability of LICOM2 in conducting high-resolution simulations and model tuning. Compared with FGOALS-g2, the simulations of both SST and Atlantic meridional overturning circulation are significantly improved in CESM1+LICOM2. The former can be mainly attributed to the atmospheric model, and the latter to the improvement in the parameterization of diapycnal mixing. The study provides a base to further improve the present version of LICOM and its functionalities in the coupled model FGOALS at both low and high resolutions.

Key words: LICOM2, CESM1, simulation, climate system, coupled model

Citation: Lin Pengfei, Liu Hailong, Xue Wei, et al., 2016: A coupled experiment with LICOM2 as the ocean component of CESM1. *J. Meteor. Res.*, **30**(1), 076–092, doi: 10.1007/s13351-015-5045-3.

1. Introduction

The LASG/IAP Climate system Ocean Model version 2 (LICOM2; Liu et al., 2012) is the ocean component of the Flexible Global Ocean-Atmosphere-Land System Model with grid-atmospheric model version 2 (FGOALS-g2; Yu et al., 2002). Recently, it was implemented in the Community Earth System Model version 1.0 (CESM1; specifically, version 1.0.4) as its oceanic component, replacing the Parallel Ocean Pro-

Supported by the National (Key) Basic Research and Development (973) Program of China (2013CB956204 and 2010CB951800), National Natural Science Foundation of China (41376019), and Strategic Priority Research Program of the Chinese Academy of Sciences (XDA11010304).

*Corresponding author: lhl@lasg.iap.ac.cn.

©The Chinese Meteorological Society and Springer-Verlag Berlin Heidelberg 2016

gram version 2 (POP2), to enhance the capabilities of LICOM2. Hereafter, we refer to the coupled model as CESM1+LICOM2.

A set of experiments has been conducted with LICOM2 under the framework of CESM1, including a stand-alone ocean model experiment (without an active sea-ice component), a Coordinated Ocean-ice Reference Experiments phase I (CORE-I) experiment, and a fully coupled experiment. The present study focuses on the simulation results from the fully coupled model; the results from the stand-alone and ocean–sea-ice coupled experiments will be reported in a separate paper. Two comparisons of the simulations were made: firstly, with observations, to evaluate the basic performance of the model; and secondly, with FGOALS-g2 (Lin et al., 2013b). Because the ocean component is almost the same as that in FGOALS-g2, except for the interface with the NCAR flux coupler version 7 (CPL7), and some updates, the effects of different atmospheric models can be inferred from the second comparison.

There were two principal motivations for implementing LICOM2 in CESM. Firstly, to meet the need for high-resolution CGCM simulations. The LASG (State Key Laboratory of Numerical Modeling for Atmospheric Sciences and Geophysical Fluid Dynamics, IAP) plans to develop a CGCM with higher resolution to conduct the experiments of the forthcoming CMIP6. The desired horizontal resolution is at least 25 km for the ocean model, and 50–100 km for the atmosphere model. However, NCAR flux coupler version 6 (CPL6), which is used in FGOALS-g2, cannot support such high-resolution simulations effectively. CPL7 has been designed to facilitate higher resolution simulations. Special efforts have been made to reduce the memory footprint and improve the memory scaling of the coupler (Craig et al., 2012). Such an advance makes it feasible to run the fully coupled system at a 10-km resolution globally. Therefore, this study can be considered as a practical and necessary first step to upgrade FGOALS from the perspective of the computational capability of a CGCM.

Secondly, LICOM has been seeking a more convenient and efficient development and tuning platform. Coupled models are usually built incrementally. That is, component models are usually developed and tuned separately or in sub-groups, such as the ocean model coupled with the sea-ice model, or the atmosphere model coupled with the land model. All these model components are then combined together to construct a fully coupled model. During the work for the Coupled Model Intercomparison Experiment (CMIP5; Taylor et al., 2012), we found that the ocean model required extensive retuning in the fully coupled model configuration, after having been initially tuned in a stand-alone configuration. Furthermore, the spatial patterns of the biases differ considerably between the ocean-only and the coupled experiments (Liu et al., 2014). We attributed this to the lack of interaction between the ocean and sea ice in the stand-alone ocean model. As pointed out by Griffies et al. (2009), the ocean–ice interaction in the polar and subpolar regions can significantly affect the global-scale ocean circulation through ice melting and formation processes, or the alteration of the fluxes entering the ocean due to the presence of sea ice. Including a sea-ice model avoids the biases caused by the introduction of the non-physical boundary conditions in the stand-alone ocean model. In hindsight, we should have tuned the ocean–sea-ice coupled model, not the ocean-only model. The Community Climate System Model version 1 (CESM1) provides both a coupled interface with other climate system components of the ocean and sea-ice models, and the observational data of the COREs. Therefore, it can be considered a convenient platform for developing and tuning individual component models and coupled models. It allows us to focus on one component only, rather than the entire coupled model, and to conduct various experiments using different sub-groups of coupled components. We consider the implementation of LICOM2 in CESM as introducing a development platform for LICOM from the perspective of an ocean modeler.

The objective of the present study was to evaluate and report the performance of CESM1+LICOM2, which is necessary for LICOM2 to be used in future coupled model simulations, including those for CMIP6 by FGOALS-g2. In-depth analyses of the physical

causes of model deficiencies are left to a future study that will compare CESM1+LICOM2 with CESM1 where the only difference is in the ocean model. Section 2 introduces CESM1+LICOM2 and describes its individual components, along with the experimental setup and data used for evaluation. The results from CESM1+LICOM2 are presented in Section 3, and Section 4 provides a summary.

2. Model description, experiments, and observation data

2.1 Model description and experiments

The basic codes of LICOM2 used here are derived from FGOALS-g2. The vertical coordinate of LICOM2 is the η-coordinate with 30 levels. The zonal resolution of LICOM2 is uniformly 1°. The meridional resolution is 0.5° between 10°S and 10°N, changing from 0.5° to 1° between 10° and 20°S/N, and 1° poleward of 20°S/N. Near the North Pole (88°–90°N), the ocean is treated as an island. The diapycnal mixing scheme is from Canuto et al. (2001, 2002). The effect of mesoscale eddies is parameterized by both Redi (1982) and Gent and McWilliams (1990). Based on Danabasoglu and McWilliams (1995), the isopycnal and thickness diffusivity coefficients are both assigned values of 500 m^2 s^{-1}.

The LICOM codes and physical processes were updated after CMIP5. Improvements were made to the parallel domain decomposition, from one dimension to two dimensions, and in introducing the tidal mixing scheme of St. Laurent et al. (2002) and the latitude-dependent background internal wave mixing diffusivity scheme of Jochum (2009). It was the updated version that was used in this study. In CESM1+LICOM2, the solar penetration scheme, dependent on the chlorophyll-a concentration (Ohlmann, 2003), is used; while in FGOALS-g2, a constant solar penetration scheme (Paulson and Simpson, 1977) was used.

CESM1 was chosen because its resolution/component combinations have been validated scientifically by NCAR (http://www.cesm.ucar.edu/models/cesm 1.0/scientific_validation.html). The oceanic, atmospheric, ice, and land components are POP2, CAM4 or CAM5 (Community Atmosphere Model version 4 or 5), CICE4 (Community Ice Code version 4), and CLM4 (Community Land Model version 4), respectively. To introduce LICOM2 into CESM1, the main program of LICOM2 has been recorded into three subroutines: the initializing, running, and finalizing programs (Li, 2013). As a result, the ocean model can be called by the flux coupler and the coupled model can become one executable file after compilation. Meanwhile, the time management of LICOM2 has also been revised to cooperate with the time management in the flux coupler.

As mentioned in the introduction, we have performed three simulations: a stand-alone ocean model experiment (without an active sea-ice component), a CORE-I experiment, and a fully coupled experiment. Here, we focus on the third of these experiments. In this experiment, the finite-volume, low-resolution (144 × 96) CAM4 was chosen for the atmospheric model. The land surface model was CLM4, with the same horizontal resolution as CAM4. The horizontal grid in the sea-ice model (CICE4) is the same as LICOM2. For the ocean model, the updated LICOM2 was used with the solar penetration scheme dependent on chlorophyll-a. The resolution of LICOM2 is the same as that in FGOALS-g2. The atmospheric chemistry and marine ecosystem and carbon cycle component were all turned off. The concentrations of greenhouse gases were set to be the preindustrial level (284 ppm for CO_2). The solar insolation in the year 1850 was used. CESM1+LICOM2 was integrated for 300 yr, starting from the annual mean observational ocean temperature and salinity from the Polar Science Center Hydrographic Climatology (PHC3.0; Steele et al., 2001). This simulation is the preindustrial control run (hereafter, PI control) under the CMIP5 protocol. Because the integration became relatively stable after 50 yr, we defined the final 50-yr average as the climatology of this experiment. The final 100 years were used to study the variability on both interannual and decadal timescales.

To understand the origin of SST biases, the CMIP5 simulations of the PI control run in FGOALS-

g2 were used to clarify the effect of the atmospheric model. Moreover, the 200-yr simulations from CESM1 with original POP2 components (denoted CESM1+POP in this paper) were carried out with the same configurations of physical parameters as those in CESM1+LICOM2. This helped to understand the effect of different oceanic components.

2.2 Observation data

As evaluation datasets, the following observational and reanalysis data were used. The ERSST.v3b (Xue et al., 2003; Smith et al., 2008) was used to construct the SST climatology. Because the PI control simulation was used for analysis, only the SST data covering the period 1854–1859 from ERSST.v3b were chosen for comparison with the climatological-mean simulations. For comparing the simulation variability, the Hadley Centre sea-ice and SST dataset (HadISST; Rayner et al., 2003) was chosen. The monthly mean sea-ice data from the Special Sensor Microwave/Image (SSM/I; Comiso, 2000) were chosen for comparison with simulated sea ice. Under the Rapid Climate Change programme (RAPID), the Atlantic meridional overturning circulation (AMOC) has been estimated observationally at 26.5°N after 2004 (Cunningham et al., 2007). The RAPID AMOC profile at this latitude was used for examining the simulation of AMOC.

The sea level pressure (SLP) and 850-hPa wind were derived from ERA-Interim data (Dee et al., 2011). The precipitation data were obtained from the Climate Prediction Center (CPC) Merged Analysis of Precipitation (CMAP; Xie and Arkin, 1997). The details of these observational and reanalysis data are listed in Table 1.

Table 1. Observation and reanalysis datasets used for comparison in this study

Variable	Dataset	Period	Reference
SST	ERSST.v3b	1854–1859	Xue et al. (2003); Smith et al. (2008)
SST	HadISST	1900–2010	Rayner et al. (2003)
Ocean temperature and salinity	PHC3.0	Before 1998	Steele et al. (2001)
Rainfall	CMAP	1980–2005	Xie and Arkin (1997)
SLP; 850-hPa wind	ERA-Interim	1989–2005	Dee et al. (2011)
Sea-ice extent	SMMR, ESMR, NIC, SSM/I	1972–2002	Cavalieri et al. (2003)
Sea-ice extent	SSM/I at NSIDC	1979–2000	Comiso (2000)
AMOC at 26.5°N	RAPID	2004–2009	Cunningham et al. (2007); Johns et al. (2011)
AMOC at 24.5° and 7.5°N	WOCE and other projects	1992–1993 2010–2011	Hernández-Guerra et al. (2014)
ACC at the Drake Passage (Sv)	Six sections along WOCE line SR1b	1993–2000	Cunningham et al. (2003)

Note: PHC: Polar Science Center Hydrographic Climatology; ESMR: Nimbus 5 Electrically Scanning Microwave Radiometer; NIC: National Ice Center; RAPID: Rapid Climate Change Programme; ACC: Antarctic circumpolar current; and SR: southern repeat.

3. Results

3.1 Long-term behavior

Relatively stable behavior was achieved in the 300-yr simulation of CESM1+LICOM2 after about 50-yr integration, according to the global-mean SST (Fig. 1a). The global-mean SST of the final 100 years is about 18.24℃, which is slightly higher than the observed value of 18℃. The stable integration behavior of SST is consistent with the very small net heat flux (the mean values are –0.07 W m^{-2} for 300 yr and –0.03 W m^{-2} for the last 100 yr, respectively) at the TOA (Fig. 1b). Because of the loss of net TOA heat flux in the model, the global volume mean temperature has a small negative trend during the 300 years (approximately 0.067℃ $(100\ yr)^{-1}$; Fig. 1c).

The stable behavior of the integration is also shown in the temporal evolution of sea-ice coverage in September and March in the NH and SH (Fig. 1d). In the NH, the sea-ice coverages in September and March

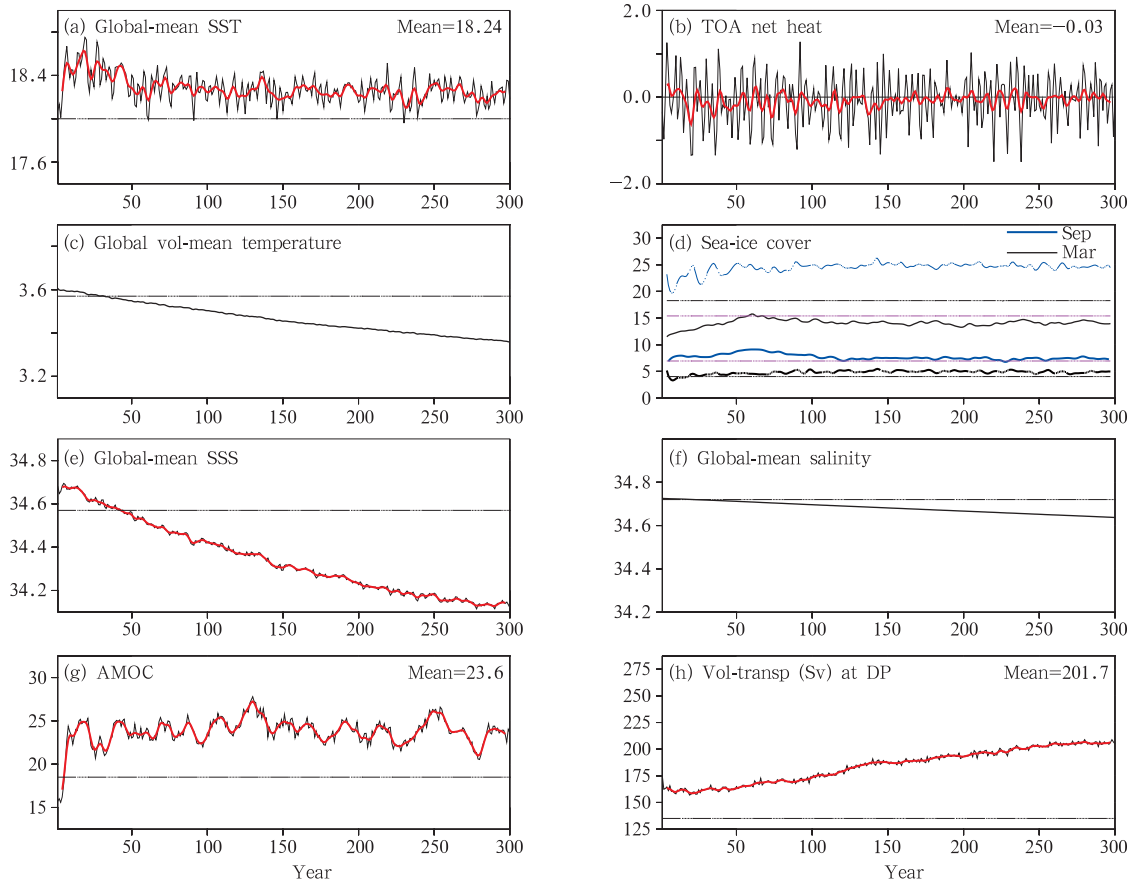

Fig. 1. Time series of (a) global-mean SST (℃), (b) net heat fluxes at the TOA (W m^{-2}), (c) global-mean ocean temperature (℃), (d) sea-ice area (million m^2) in September and March in the NH and SH, (e) global-mean sea surface salinity (SSS; psu), (f) global-mean salinity (psu), (g) AMOC averaged from 900 to 1200 m at 26.5°N (Sv, 1 Sv = 10^6 m^3 s^{-1}), and (h) volume transport at Drake Passage (Sv), in the PI control run simulated by CESM1+LICOM2. The thick red lines indicate the 9-yr running mean values. The thick lines (blue and black dashed lines) in (d) represent sea-ice cover in the NH (SH). The purple dashed and light black lines in (d) are for the observed values.

are both close to the observations (Cavalieri et al., 2003). In the SH, the sea-ice coverage in March is close to the observation; whereas in September (25 million km^2), it is larger than observed, which is related to the SST being too cold.

An obvious drift exists in the sea surface salinity (SSS) (Fig. 1e). This is due to the net input of freshwater flux at the sea surface (figure omitted), which reduces the global volume mean salinity in the ocean (Fig. 1f). The inconsistent changes of the trend in SSS and global volume mean salinity result from the redistribution of salinity in the vertical direction.

There is no obvious drift in the simulated AMOC (Fig. 1g). The AMOC value (23.6 Sv) is nearly 25% larger than that in a recent estimation from direct observation (18.7 Sv; Cunningham et al., 2007). In the NH, the reasonable simulation of sea-ice coverage may be related to the well-simulated AMOC. The overly strong transport of the Antarctic circumpolar current (ACC) (201.7 Sv; 135 Sv in the observation from Cunningham et al., 2003) and its gradually increasing trend can affect the sea ice in the SH. In the SH, the overly cold SST may be connected with the overly strong ACC, as shown later in the wind and SLP fields.

These stable evolution behaviors of global mean SST, TOA, sea-ice cover, AMOC, and ACC are comparable with those in FGOALS-g2 (Lin et al., 2013a).

However, the global-mean values of these variables are different, such as the colder and warmer SST, larger and smaller absolute magnitude of the TOA, and the much larger and slightly larger ACC than observed for FGOALS-g2 and CESM1+LICOM2, respectively (figure omitted). In addition, similar evolutions of global volume mean temperature are apparent. The evolutions of global volume mean salinity are increasing and deceasing gradually for FGOALS-g2 and CESM1+LICOM2, respectively.

3.2 Mean state

3.2.1 Ocean

Figure 2 shows the annual-mean SST for CESM1+LICOM2 and the SST difference between the simulation and ERSST.v3b during 1854–1859. The RMSE is 1.1℃ for CESM1+LICOM2 against the observation. The spatial pattern of the SST bias in CESM1+LICOM2 is similar to that in CCSM4 (Gent et al., 2011) and the CMIP5 ensemble mean (Wang et

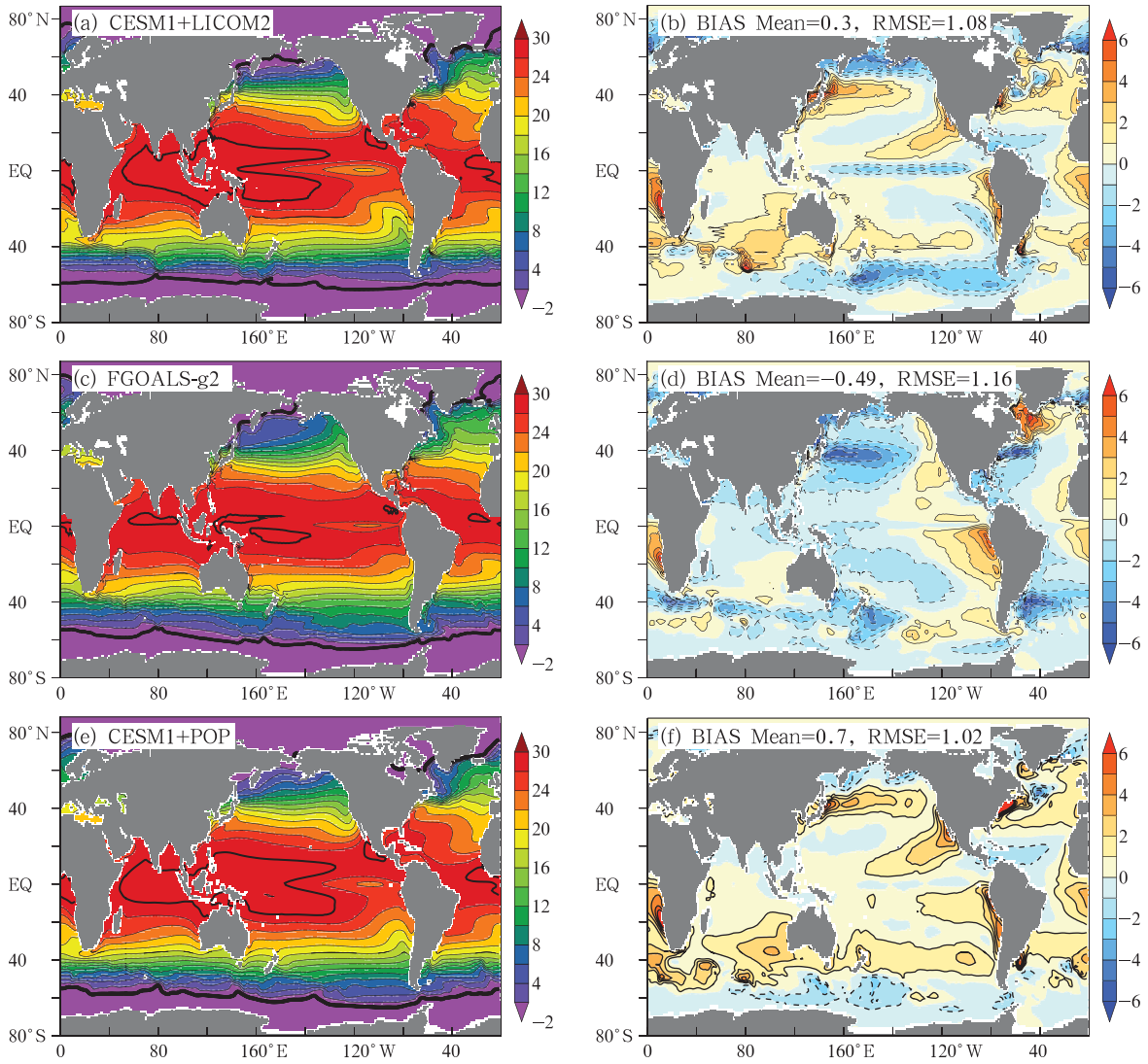

Fig. 2. (a) Annual mean SST (℃) in the PI control run simulated by CESM1+LICOM2, and (b) the SST difference (℃) between the simulation and observations from ERSST during 1854–1859. Panels (c, d) are similar to (a, b), respectively, but simulated by FGOALS-g2. Panels (e, f) are similar to (a, b), respectively, but simulated by CESM1+POP. Thick lines in (a) indicate the 28℃ or 0℃ isotherms.

al., 2014).

In CESM1+LICOM2, the warm SST biases appear mainly along the oceanic eastern coast and around the strong western boundary currents (e.g., in North Pacific between 20° and 50°N, and in most areas of North Atlantic between 30° and 60°N). The cold biases (< –2℃) are located mainly in the equatorial central and eastern Pacific cold tongue, the tropical western Atlantic, the Barents Sea, the region northeast of Iceland, and the Pacific Ocean sector of the Southern Ocean. Many of these biases are also in the CMIP5 ensemble mean (Wang et al., 2014), including the warm biases along the oceanic eastern coast and cold biases in the Pacific cold tongue and the tropical western Atlantic. However, the cold biases in the Pacific Ocean sector of the Southern Ocean and the warm biases around the strong western boundary currents are different from those in the CMIP5 ensemble mean (Wang et al., 2014).

Compared with the previous version of the LASG's coupled model (FGOALS-g2), we found that the cold biases are significantly reduced. The spatial RMSE in CESM1+LICOM2 is also slightly smaller than that in FGOALS-g2 (1.2℃; Fig. 2d). The global mean SST in FGOALS-g2 is only 17.5℃, which is about 0.5℃ colder than in the observations (Figs. 2c and 2d). The Indo-Pacific warm pool, which is usually defined by a region within the 28℃ isotherms, is much larger and more realistic in CESM1+LICOM2 than that in FGOALS-g2 (Figs. 2a and 2c), especially in the equatorial Indian Ocean. The cold biases (< –4℃) centered at 40°N in North Pacific in FGOALS-g2 have been replaced by warm biases in CESM1+LICOM2. The changes are most likely due to the different atmospheric components. In North Atlantic, south of 60°N, the biases are reduced significantly in CESM1+LICOM2 compared with FGOALS-g2. Such an improvement may be associated with the more reasonable AMOC simulation in CESM1+LICOM2 than in FGOALS-g2, which will be further discussed in the following. All these changes contribute to the reduction of the cold bias in the global-mean SST of CESM1+LICOM2. However, there are places in CESM1+LICOM2 where the cold bias is larger than in FGOALS-g2, most evidently in the equatorial central and eastern Pacific. The seasonal chlorophyll distribution may contribute to the cold bias by about 0.5–1℃ (Lin et al., 2011).

There are similar distributions of SST biases with different magnitudes in CESM1+LICOM2 and CESM1+POP due to similar spatial RMSE (Figs. 2b and 2f). This indicates the similar SST bias patterns are determined by other component models, particularly the atmospheric model, and apart from the ocean component. Globally, the mean SST, with a bias of 0.3℃ in CESM1+LICOM2, is closer to the observed than that in CESM1+POP, with a bias of 0.7℃, since the local SST in CESM1+LICOM2 is colder than that in CESM1+POP in most regions, except the North Indian Ocean, tropical Atlantic Ocean, and North Atlantic Ocean. This tells us that bias magnitudes can be greatly affected by different ocean models. Furthermore, compared with CESM1+POP, the SST cold biases in CESM1+LICOM2 are more significant in the equatorial Pacific, the Southern Ocean between 45° and 75°S, North Pacific between 50° and 60°N, and the Barents Sea. In these dynamic ocean regions, the biases due to different ocean models are significant and need to be investigated further.

Figure 3 shows the global MOC and AMOC for CESM1+LICOM2 and FGOALS-g2, and the simulated and observed vertical profiles of the volume transport along 26.5°N. The pattern of global MOC is captured well by CESM1+LICOM2 (Fig. 3a), in comparison with those results from the schematic diagram and the tracer inversion methods (Lumpkin and Speer, 2007; Marshall and Speer, 2012; Liu and Liu, 2014). In the CESM1+LICOM2 simulation, the magnitudes of volume transport by the North Atlantic Deep Water (NADW) and Antarctic Bottom Water (AABW) are about 24 and 10 Sv, respectively.

The depth of the maximal magnitude of NADW at 26.5°N is the same as the observations at around 1000 m (Fig. 3e). The maximal magnitude of NADW in CESM1+LICOM2 (about 24 Sv) is about 30% larger than that observed, which is about 18.7 Sv for the 1-yr record from Cunningham et al. (2007) and about 18.5 Sv for the 3.5-yr record from Johns et

al. (2011). At 24.5° and 7.5°N, the simulated values are about 22 and 20 Sv, which are within the ranges of observed values (20.1–24.7 and 16.9–29.2 Sv, respectively) estimated by Hernández-Guerra et al. (2014). The simulated NADW for CESM1+LICOM2 at 26.5°N can extend to 3500 m, but it remains about 1000 m shallower than observed.

In FGOALS-g2, the magnitude of volume trans-

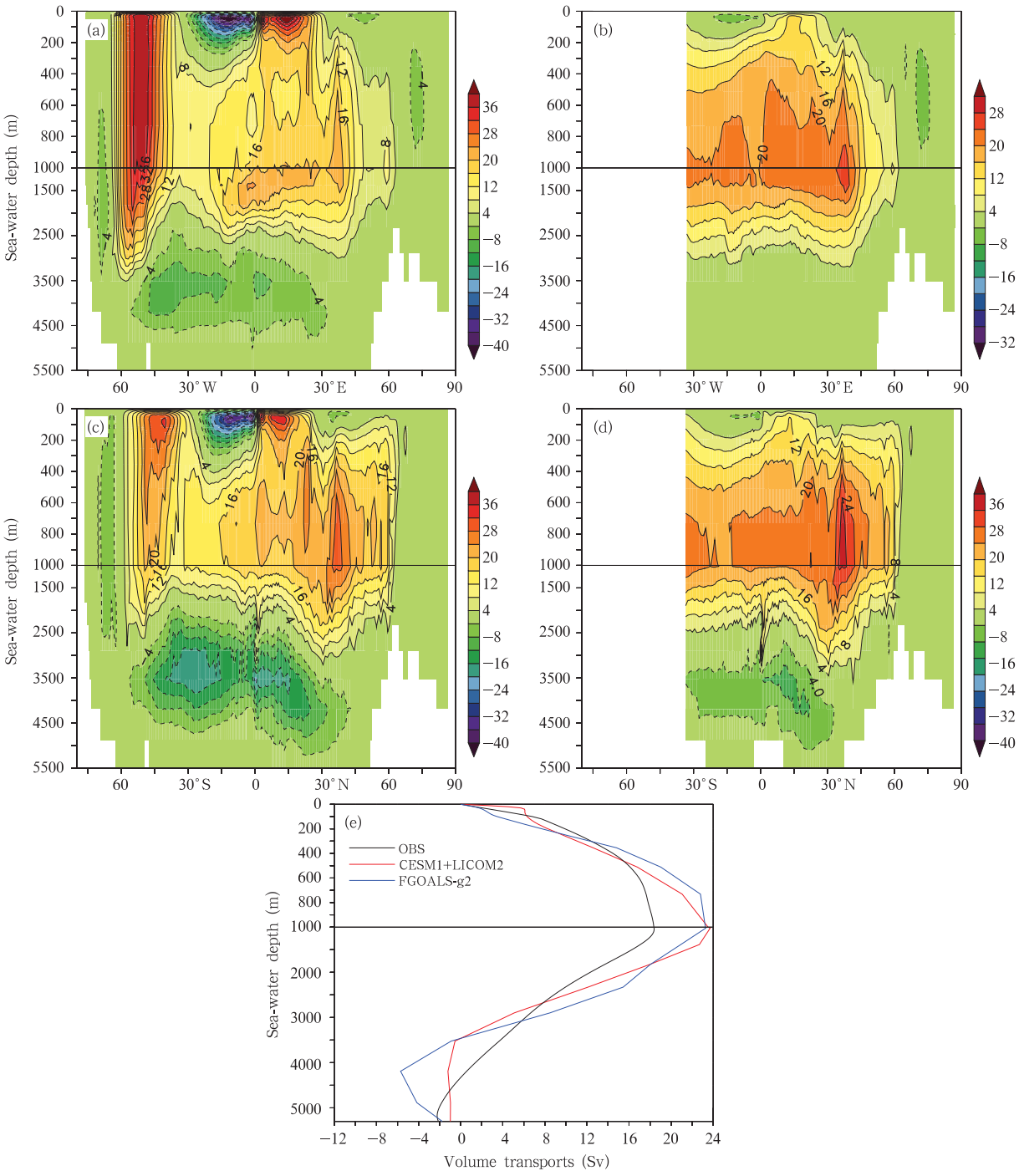

Fig. 3. MOC (Sv) in the PI control run simulated by CESM1+LICOM2: (a) globe and (b) Atlantic. Panels (c, d) are similar to (a, b) but for that simulated by FGOALS-g2. (e) The simulated (red line for CESM1+LICOM2 and blue line for FGOALS-g2) and observed (black line) volume transports (Sv) at 26.5°N.

port by NADW is 28 Sv, which is 4 Sv larger than that in CESM1+LICOM2 (Figs. 3c and 3d). The NADW extends to 200–500 m deeper in CESM1+LICOM2 (the value of 4 Sv reaching the depth of 3500 m at around 30°N) than in FGOALS-g2 (the value of 4 Sv reaching the depth of 3000 m at around 30°N). In addition to the deeper extension of the NADW for CESM1+LICOM2, the most evident difference between CESM1+LICOM2 and FGOALS-g2 is the much larger transport of AABW in the simulation of the latter. The maximal value of volume transport of AABW is about 6 Sv at 26.5°N for FGOAL-g2, while is only about 1 Sv for CESM1+LICOM2 (Fig. 3e), which is much closer to observations. CESM1+LICOM2 uses tidal mixing, while FGOALS-g2 does not. We found that the simulation of NADW is significantly improved after the introduction of the tidal mixing scheme (figures omitted). Thus, the improvements in both the vertical structure and the magnitude of AMOC in CESM1+LICOM2 can be mainly attributed to the improvement in the parameterization of diapycnal mixing in the ocean component.

In the Southern Ocean, the strong circulation from the surface to 3500 m deep is called the Deacon Cell. The maximal magnitude of the Deacon Cell can exceed 36 Sv, which is nearly 4 Sv larger than that in FGOALS-g2 (Lin et al., 2013b). The larger Deacon Cell for CESM1+LICOM2 is related to the strong ACC.

3.2.2 Sea ice

The spatial distributions of sea-ice concentration (SIC) and sea-ice thickness in March and September in CESM1+LICOM2 are shown in Fig. 4. March and September are also the months in which the seasonal maximum (minimum) and minimum (maximum) of SIC occur for the NH (SH). The simulation captures the observed SIC distributions (Comiso, 2000) in the NH well, which shows that most of the Arctic Ocean and the high-latitude oceans are covered by sea ice in March, while the sea-ice extent reduces and retreats to the Arctic Ocean in September. It is important to point out that the simulation somewhat overestimates the SIC over the Barents Sea and Bering Sea, and underestimates the SIC over the Labrador Sea and Hudson Bay in March (Figs. 4a and 4b).

In the SH, the observation shows the SIC in March exists near Antarctica only, with the maximum amount in the southwest of the Weddell Sea. SIC increases considerably in September, such that the Southern Ocean south of 60°S is almost entirely covered by sea ice in the observations. The main characteristics of Antarctic SIC in March and September are reflected well in the simulation, although the northward extension of SIC in the Southern Ocean is overestimated in September.

Figures 4e and 4f illustrate the seasonal distribution of sea-ice thickness in the NH. The thickest sea ice (up to 5–6 m) is over areas to the north of the Canadian Archipelago and Greenland; sea ice becomes thinner toward the coast of the Eurasian continent, with ice thicknesses of less than 1 m adjacent to the Russian coast, which is very close to the observations (Morison and Andersen, 1998). However, extremely low SIC ($< 1\%$) with ice thickness (< 0.5 m) is simulated by CESM1+LICOM2 near the sea-ice edge zone in North Pacific, North Atlantic, and Southern Ocean. These features are not found in observations.

The simulated distribution of sea-ice thickness by CESM1+LICOM2 in the NH is closer to observed than that by FGOALS-g2 (figure omitted). The thickest ice occurs over the North Pole in FGOALS-g2, while in observations it is located to the north of the Canadian Archipelago and Greenland. The improvement may be related to the change in atmosphere state and circulation.

3.2.3 Atmosphere

Figure 5 shows the annual mean SLP and wind vectors at 850 hPa. Overall, the atmospheric general circulations are simulated well in CESM1+LICOM2, although in the tropics and subtropics the low and high pressure are underestimated and overestimated, respectively, compared with the reanalysis data. In the subpolar region, the low pressure is underestimated in CESM1+LICOM2. These patterns are similar to results from FGOALS-g2 (figure omitted).

The easterly winds at 850 hPa are stronger than those in ERA-Interim data in the tropics, which may be associated with the overly cold SST in the central-

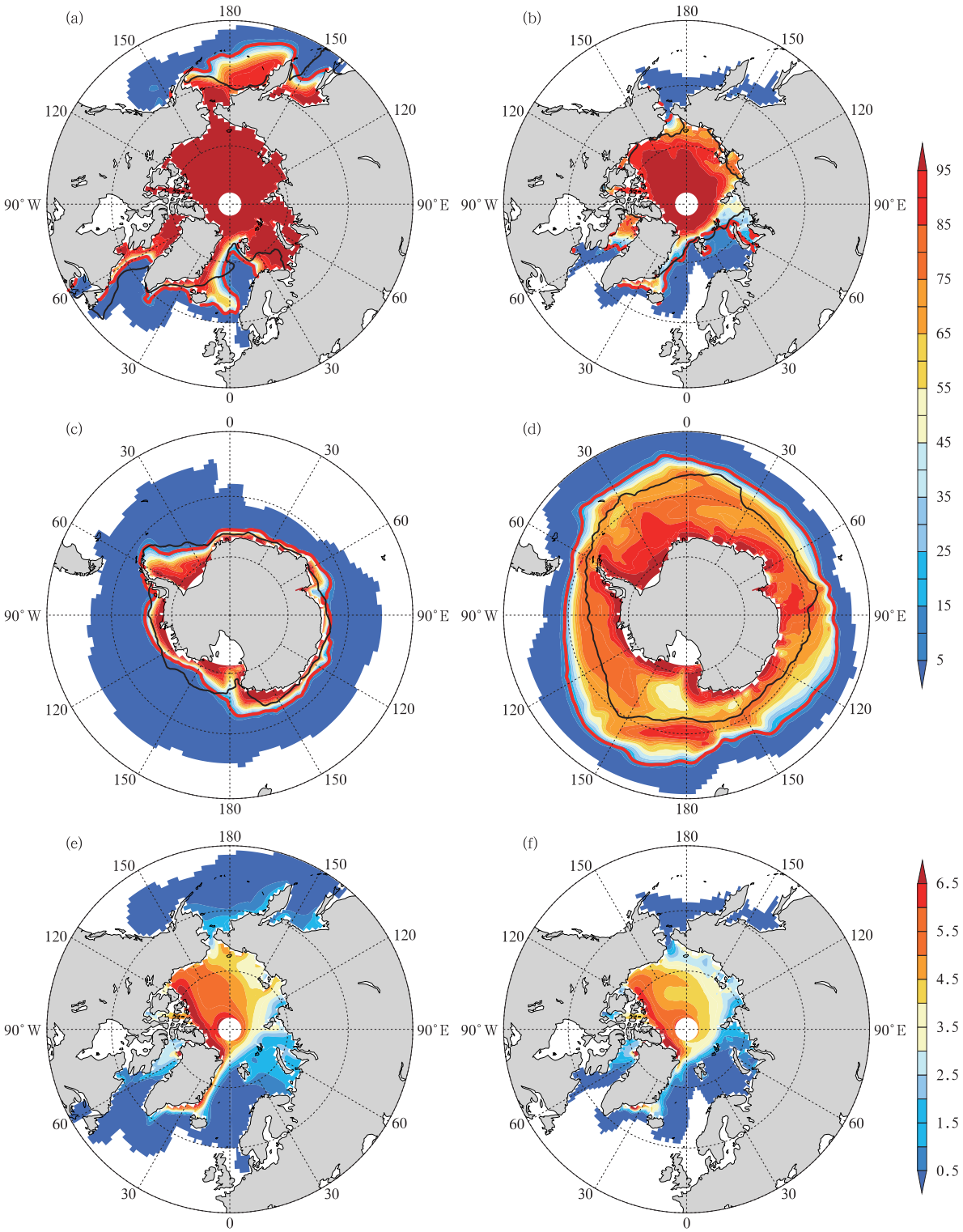

Fig. 4. Simulated SIC (%) in (a, c) March and (b, d) September in the NH and SH, respectively. The simulated and observed 15% SIC is denoted by the purple and dark thick lines, respectively. (e, f) Simulated sea-ice thickness (m) in March and September, respectively, in the NH.

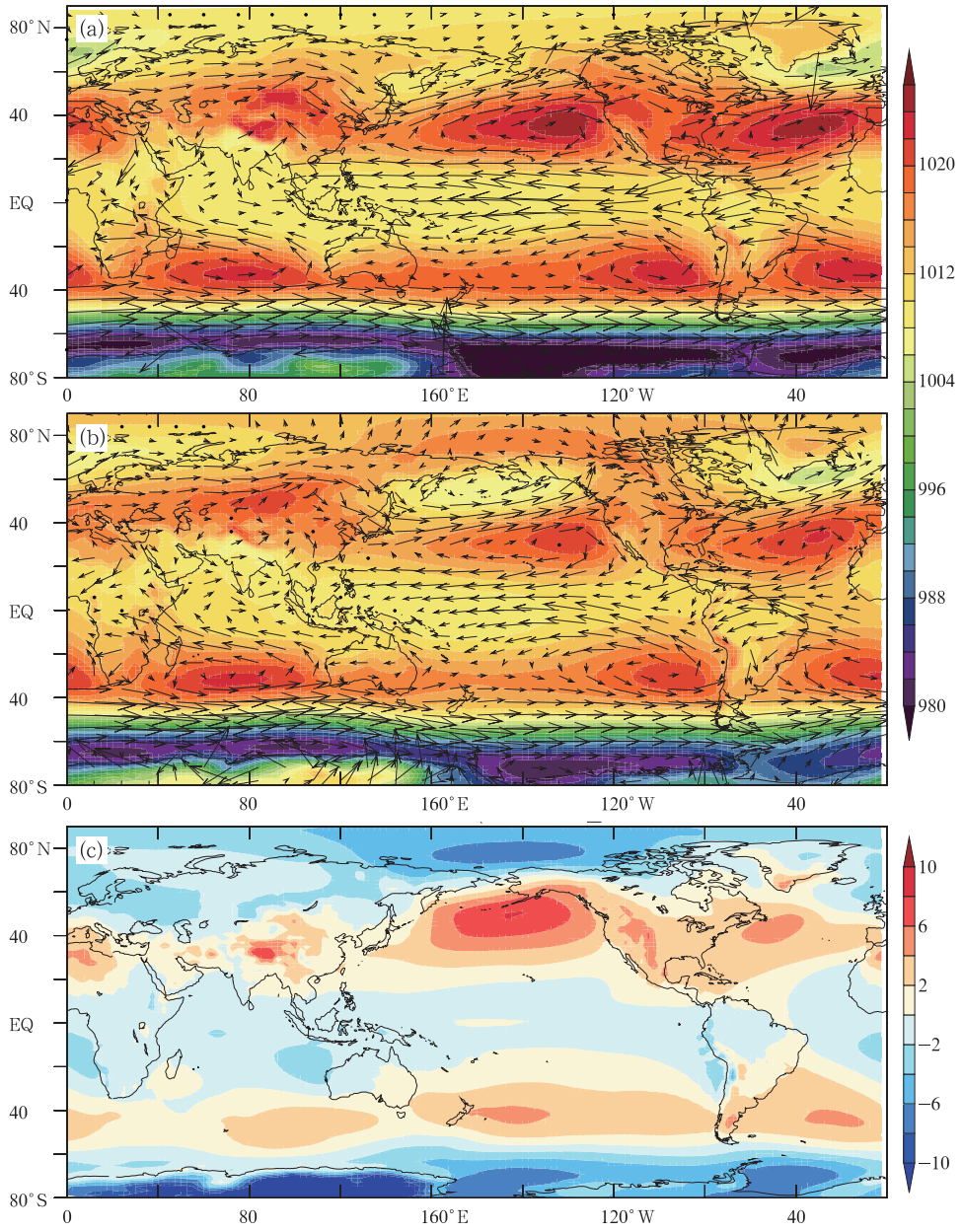

Fig. 5. SLP (hPa; shaded) and wind (m s^{-1}; vectors) at 850 hPa from (a) simulation and (b) observations. (c) SLP difference between the simulation and observations (i.e., simulation minus observations).

eastern Pacific. In the high latitudes south of 40°S, the westerly winds in the simulation are located further to the south than in the reanalysis.

In CESM1+LICOM2, the main rain belts are generally reproduced (Figs. 6a and 6b). The global annual mean bias is 0.18 mm day^{-1} and the spatial RMSE is 0.84 mm day^{-1}. The largest biases of precipitation occur in the tropics. The southern branch of the ITCZ extends too far eastward in both the Pacific and Atlantic basins, and runs parallel to the equator. This is a common bias for directly coupled models and is referred to as the "double ITCZ" bias (e.g., Zhang et al., 2007). The simulated northern branch of the ITCZ is too broad and too strong in the central Pacific. The lower rainfall in the central equatorial Pacific is related to the colder SST bias there (Fig. 2). In the western

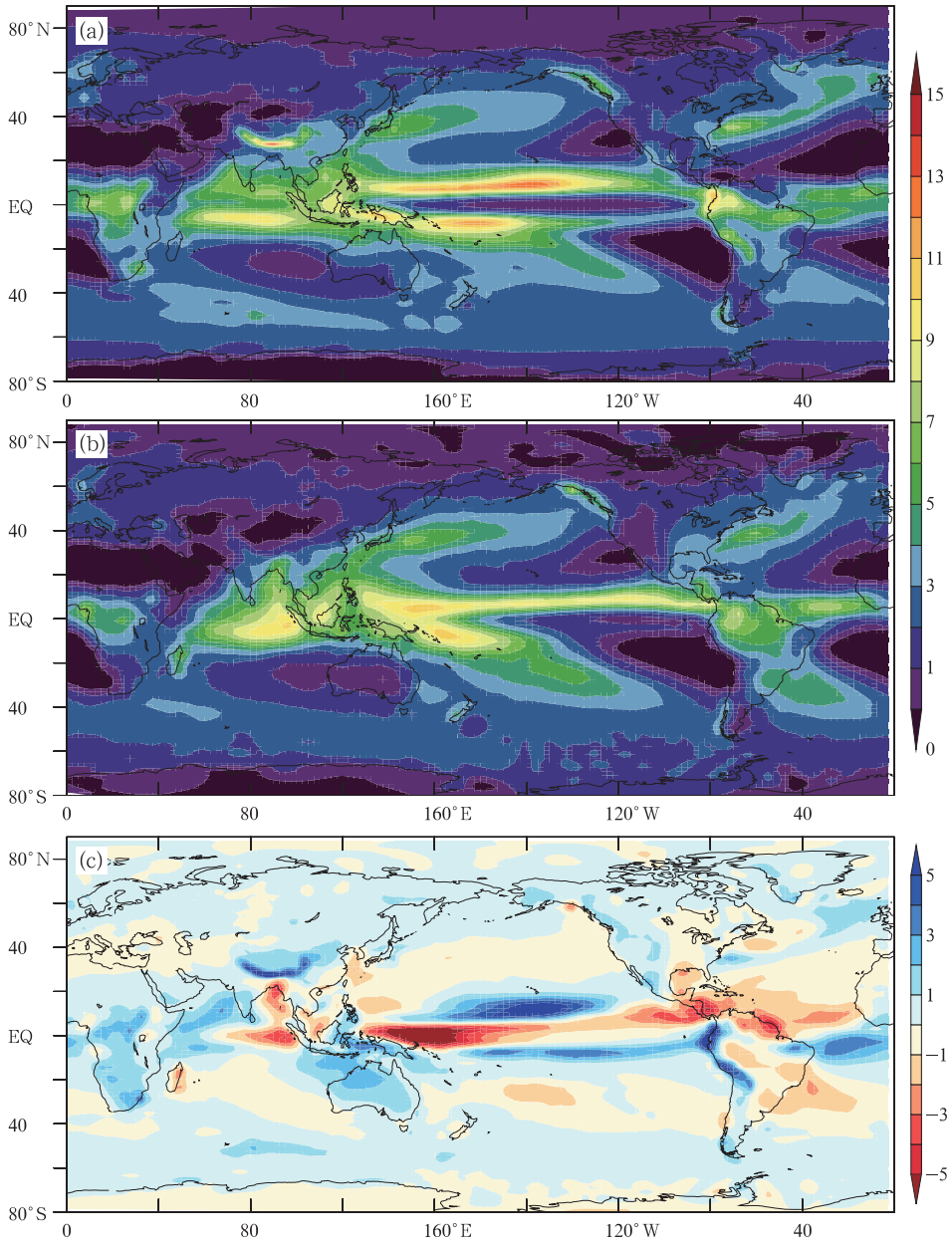

Fig. 6. Annual mean rainfall (mm day^{-1}) for (a) CESM1+LICOM2 and (b) observations, and (c) difference between the simulation and observations.

(eastern) Indian Ocean, the rainfall is overestimated (underestimated). Besides the tropical region, excessive precipitation can also be found in the southern parts of the Tibetan Plateau. These rainfall biases are comparable to those in CCSM4 (Gent et al., 2011).

3.3 ENSO and Pacific decadal oscillation

We also evaluated the interannual and decadal variabilities in the CESM1+LICOM2 simulation; specifically, ENSO and Pacific decadal oscillation (PDO). Before presenting the simulated ENSO by CESM1+LICOM2, we first show the seasonal variation of the climatological monthly SST anomaly, averaged between 2°S and 2°N, in Fig. 7. The annual cycle in the eastern equatorial Pacific and the semi-annual cycle in the western equatorial Pacific are simulated

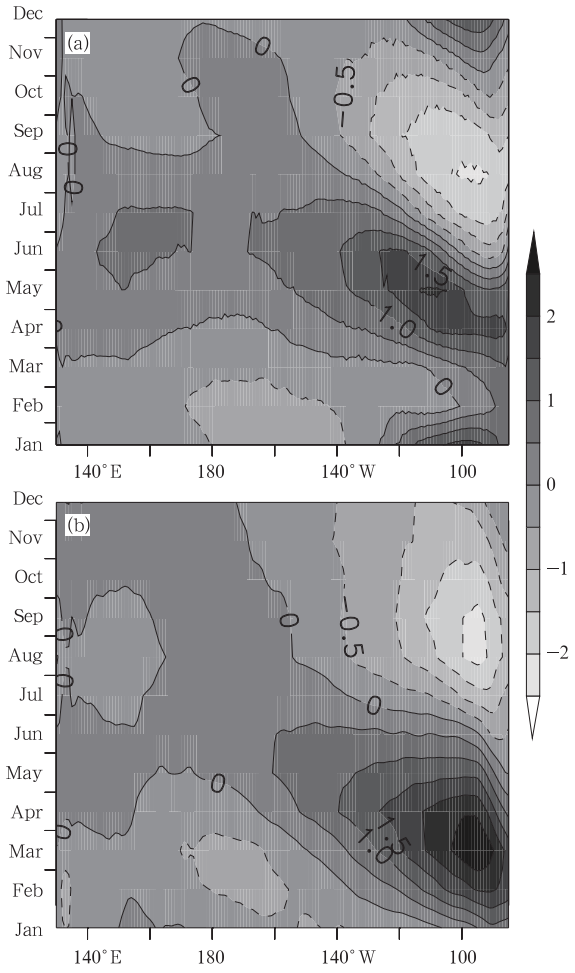

Fig. 7. SST seasonal evolution averaged between 2°S and 2°N in the Pacific for (a) simulation and (b) observations.

well (Figs. 7a and 7b). The westward propagation of the SST anomaly is also comparable with the observations, although the phase of the seasonal cycle in the eastern Pacific has a lag of about one month. The maximal warming appears during May–June in the model, while it is during March–April in the observations. The model simulated warming during December–January, followed by some slight cooling during February–March, which registers a semi-annual signal in the eastern Pacific. The seasonal evolution of the SST anomaly is similar to that in CCSM4 (Gent et al., 2011), even though the ocean model is different.

To examine the interannual variation in CESM1+LICOM2, we show the pattern of SST monthly mean anomalies regressed onto the Niño3.4 index (Fig. 8), the monthly standard deviation of the Niño3.4 index, and the power spectrum of the Niño3.4 index. In general, the overall pattern of the regression coefficient is similar to that in the observations. However, the pattern in the Indo-Pacific basin shifts by 10° westward (Figs. 8a and 8b), possibly related to the overly cold and westward extension of the equatorial cold tongue (Fig. 2). The amplitude of ENSO in CESM1+LICOM2, in terms of the Niño3.4 index, is nearly twice that in the observations. Strong ENSO signals can be found in the monthly standard deviation and the spectrum of the Niño3.4 index (Figs. 8c–f). The seasonal phase lock of ENSO is reproduced by the model, with the maximal standard deviation in boreal winter (Figs. 8c and 8d). As in the observation, CESM1+LICOM2 also has relatively broad spectrum peaks within the interannual timescale of 2–7 yr (Figs. 8e and 8f).

Figure 9 shows the spatial pattern and the time series of the first mode of the SST monthly mean anomalies in North Pacific for both CESM1+LICOM2 and HadISST, which are often used to represent the PDO (Mantua et al., 1997). The spatial pattern of the PDO is simulated well by CESM1+LICOM2. Two features of the model are different from the observations. Firstly, the magnitude of the simulated result is 30%–50% larger than that of the observations, while the magnitude in FGOALS-g2 is closer to that of the observations but with slightly larger magnitude. Secondly, the center of the negative value shifts westward, similar to the pattern of the interannual variability. A westward-shifted center can also be seen in FGOALS-g2. This may be related to the much broader western boundary currents due to the coarse resolution of the ocean model. The time series of the first principal component shows that the period of the PDO for CESM1+LICOM2 is shorter than that in the observations. However, the period of the PDO in FGOALS-g2 is comparable to that observed (Zhou et al., 2014). Meanwhile, the ENSO amplitude in FGOALS-g2 is weaker than that in CESM1+LICOM2 and is comparable to that observed (Li et al., 2013). These comparisons suggest that the strong ENSO amplitudes may result in a tendency for the PDO periods

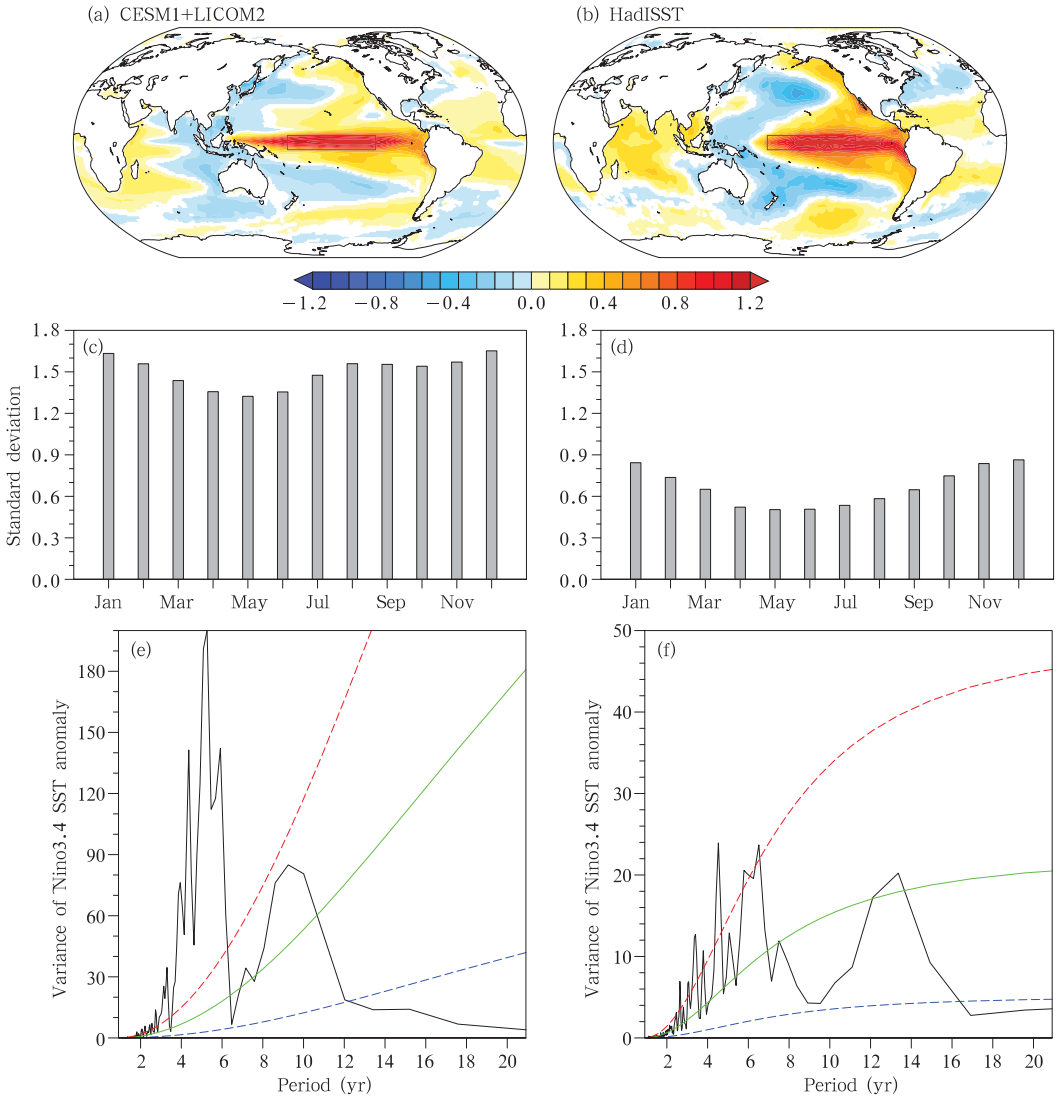

Fig. 8. (a, b) Regression of the SST anomaly onto the Niño3.4 index (℃), (c, d) standard deviation and (e, f) power spectrum of the Niño3.4 SST anomaly (℃), in the (a, c, e) simulation by CESM1+LICOM2 and (b, d, f) observations. The green, red, and blue lines are the significant test lines from the red noise and the upper and lower confidence lines, respectively.

to be shorter because of the important role of ENSO in climate oscillation globally, especially in the Pacific. In addition, the PDO time series show less noise in CESM1+LICOM2 compared with that in the observations and FGOALS-g2. The reason for this is unclear.

4. Summary and discussion

In the present study, the oceanic component of CESM1 was replaced by the latest version of LICOM. A 300-yr PI control experiment has been conducted using this coupled model (CESM1+LICOM2), and its baseline performance evaluated against both observations and the previous version of the LASG coupled model.

CESM1+LICOM2 has been stably integrated without obvious climatic drift over 300 model years. The mean features of the ocean, sea ice, and atmosphere are simulated well with CESM1+LICOM2, relative to the performance of FGOALS-g2 and the CMIP5 multi-model ensemble mean. The SST bias in CESM1+LICOM2 is similar to that in CCSM4 in its

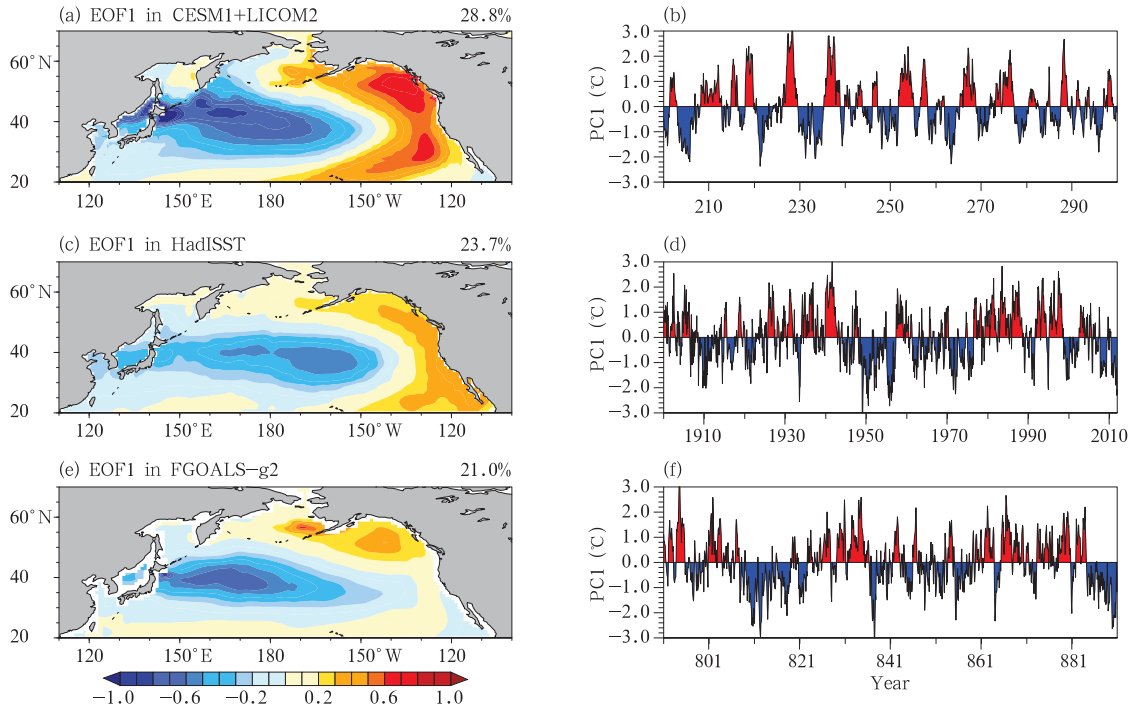

Fig. 9. (a) First EOF mode and (b) its standardized principal component in North Pacific for the simulation by CESM1+LICOM2. (c, d) As in (a, b), but for the observations. (e, f) As in (a, b), but for the simulations by FGOALS-g2.

spatial pattern, indicating a primary source beyond the ocean model, but with different magnitude. The simulated climate variability, such as ENSO and PDO, are comparable with those of the observations. This indicates that the replacement of POP2 by LICOM2 has been successful in the CESM1 framework, and CESM1+LICOM2 can be used as coupled climate model with a different ocean component from CESM1. In future work, we will extend this experiment to a simulation of around 1000 model years, and evaluate the results.

Compared with those of the multi-model CMIP5 ensemble mean (Wang et al., 2014), the warm biases in the SST along the oceanic eastern coast, and the cold biases in the Pacific cold tongue and tropical western Atlantic are common to the CMIP5 model ensemble mean and CESM1+LICOM2. Different to the CMIP5 ensemble mean, however, the cold biases in the Pacific Ocean sector of the Southern Ocean and the warm biases around the strong western boundary currents are unique in CESM+LICOM2 and CCSM4, albeit different magnitudes are achieved. Similar atmospheric, land, and sea-ice models (CAM4, CLM4, and CICE4), and similar SST bias distributions, suggest that the mean SST bias distributions are determined by other component models aside from the ocean component. The ocean component can affect the magnitude of global-mean SST bias, and a number of biases in some ocean dynamical active regions, such as the equatorial Pacific, in the Southern Ocean between 45° and 75°S, in North Pacific between 50° and 60°N, and in the Barents Sea. From another viewpoint, because similar simulation abilities are achieved in CCSM4 and CESM1+LICOM2, LICOM2 can act as an ocean component of CESM1 besides POP2.

Several important improvements are apparent in CESM1+LICOM2 relative to FGOALS-g2, especially with respect to SST. The cold biases in the global-mean SST in FGOALS-g2 are significantly reduced. The global mean SST is 0.23℃ warmer for CESM1+LICOM2, and 0.6℃ colder for FGOALS-g2, than that of observations. Furthermore, the spatial SST biases for CESM1+LICOM2 are smaller than those for FGOALS-g2. The Indo-Pacific warm

pool in CESM1+LICOM2 is much larger than that in FGOALS-g2, and more realistic, especially in the Indian Ocean. The cold biases (< –4℃) centered at 40°N in the North Pacific for FGOALS-g2 have been replaced by warm biases. In the North Atlantic (south of 60°N), the biases of SST are significantly reduced in CESM1+LICOM2. The improvements in the SST distribution may lead to improvements in sea-ice cover in the NH.

The representations of the vertical structures and magnitudes of the AMOC and AABW are also more reasonable in CESM1+LICOM2 than in FGOALS-g2. These improvements can be mainly attributed to the improvement in the parameterization of diapycnal mixing, by adopting a tidal mixing scheme, in LICOM2. This will lead to an improvement of the simulated SST and sea-ice distributions in the NH.

Future work will focus on the differences in the coupled simulations in CESM1+LICOM2 and CESM1, to understand the role of ocean models in accounting for model biases. This will help us further improve our model. Additionally, a CORE II experiment is also planned, in which we will make comparisons with other ocean models under the same prescribed atmospheric forcing to understand the forced variabilities and their underlying mechanisms. The study lays a foundation for further development of LICOM and its coupling with other components in the low/high resolution FGOALS coupled climate models.

Acknowledgments. The authors are grateful to the two anonymous reviewers for their constructive comments, which helped to improve this paper.

REFERENCES

Canuto, V. M., A. Howard, Y. Cheng, et al., 2001: Ocean turbulence. Part I: One-point closure model–Momentum and heat vertical diffusivities. *J. Phys. Oceanogr.*, **31**, 1413–1426.

Canuto, V. M., A. Howard, Y. Cheng, et al., 2002: Ocean turbulence. Part II: Vertical diffusivities of momentum, heat, salt, mass, and passive scalars. *J. Phys. Oceanogr.*, **32**, 240–264.

Cavalieri, D. J., C. L. Parkinson, and K. Y. Vinnikov, 2003: 30-year satellite record reveals contrasting Arctic and Antarctic decadal sea ice variability. *Geophys. Res. Lett.*, **30**, doi: 10.1029/2003GL018031.

Comiso, J. C., 2000 (updated 2015): Bootstrap Sea Ice Concentrations from Nimbus-7 SMMR and DMSP SSM/I-SSMIS, Version 2. Boulder, Colorado USA. NASA National Snow and Ice Data Center Distributed Active Archive Center. http://dx.doi.org/10.5067/J6JQLS9EJ5HU.

Craig, A. P., M. Vertenstein, and R. Jacob, 2012: A new flexible coupler for earth system modeling developed for CCSM4 and CESM1. *International Journal of High Performance Computing Applications*, **26**, 31–42, doi: 10.1177/1094342011428141.

Cunningham, S. A., S. G. Alderson, B. A. King, et al., 2003: Transport and variability of the Antarctic circumpolar current in Drake passage. *J. Geophys. Res.*, **108**, 8084, doi: 10.1029/2001JC001147.

Cunningham, S. A., T. Kanzow, D. Rayner, et al., 2007: Temporal variability of the Atlantic meridional overturning circulation at 26°N. *Science*, **317**, 935–938, doi: 10.1126/science.1141304.

Danabasoglu, G., and J. C. McWilliams, 1995: Sensitivity of the global ocean circulation to parameterizations of mesoscale tracer transports. *J. Climate*, **8**, 2967–2987.

Dee, D. P., S. M. Uppala, A. J. Simmons, et al., 2011: The ERA-Interim reanalysis: Configuration and performance of the data assimilation system. *Quart. J. Roy. Meteor. Soc.*, **137**, 553–597, doi: 10.1002/qj.828.

Gent, P. R., and J. C. McWilliams, 1990: Isopycnal mixing in ocean circulation models. *J. Phys. Oceanogr.*, **20**, 150–155.

Gent, P. R., G. Danabasoglu, L. J. Donner, et al., 2011: The community climate system model version 4. *J. Climate*, **24**, 4973–4991, doi: 10.1175/2011JCLI4083.1.

Griffies, S. M., A. Biastoch, C. Böning, et al., 2009: Coordinated ocean-ice reference experiments (COREs). *Ocean Modeling*, **26**, 1–46.

Hernández-Guerra, A, J. L. Pelegrí, E. Fraile-Nuez, et al., 2014: Meridional overturning transports at 7.5° and 24.5°N in the Atlantic Ocean during 1992–93 and 2010–11. *Progress Oceanogr.*, **128**, 98–114.

Jochum, M., 2009: Impact of latitudinal variations in vertical diffusivity on climate simulations. *J. Geophys. Res.*, **114**, C01010, doi: 10.1029/2008JC005030.

Johns, W. E., M. O. Baringer, L. M. Beal, et al., 2011: Continuous, array-based estimates of Atlantic Ocean heat transport at 26.5°N. *J. Climate*, **24**, 2429–2449.

Li Huimin, 2013: Coupled ensemble platform and performance model for climate system model. Master Thesis, Tsinghua University, China, 81 pp. (in Chinese)

Lin Pengfei, Liu Hailong, Yu Yongqiang, et al., 2011: Response of sea surface temperature to chlorophyll-a concentration in the tropical Pacific: Annual mean, seasonal cycle, and interannual variability. *Adv. Atmos. Sci.*, **28**, 492–510.

Lin Pengfei, Liu Hailong, Yu Yongqiang, et al., 2013a: Long-term behaviors of two versions of FGOALS2 in the preindustrial control simulations with implications for the 20th century simulations. *Adv. Atmos. Sci.*, **30**, 577–592.

Lin Pengfei, Yu Yongqiang, and Liu Hailong, 2013b: Oceanic climatology in the coupled model FGOALS-g2: Improvements and biases. *Adv. Atmos. Sci.*, **30**, 819–840, doi: 10.1007/s00376-012-2137-1.

Liu Hailong, Lin Pengfei, Yu Yongqiang, et al., 2012: The baseline evaluation of LASG/IAP Climate system Ocean Model (LICOM) version 2. *Acta Meteor. Sinica*, **26**, 318–329.

Liu, H. L., Y. Q. Yu, P. F. Lin, et al., 2014: Chapter 38 High-Resolution LICOM. *Flexible Global Ocean–Atmosphere–Land System Model: A Modeling Tool for the Climate Change Research Community.* Zhou, T. J., et al., Eds., Springer-Verlag, Berlin Heidelberg, 321–331, doi: 10.1007/978-3-642-41801-3_38.

Liu Wei and Liu Zhengyu, 2014: Assessing the stability of the Atlantic meridional overturining circulation of the past, present, and future. *J. Meteor. Res.*, **28**, 803–819.

Lumpkin, R., and K. Speer, 2007: Global ocean meridional overturning. *J. Phys. Oceanogr.*, **37**, 2550–2562.

Mantua, N. J., S. R. Hare, Y. Zhang, et al., 1997: A Pacific decadal climate oscillation with impacts on salmon. *Bull. Amer. Meteor. Soc.*, **78**, 1069–1079.

Marshall, J., and K. Speer, 2012: Closure of the meridional overturning circulation through Southern Ocean upwelling. *Nat. Geosci.*, **5**, 171–180, doi: 10.1038/ngeo1391.

Morison, J., M. Steele, and R. Andersen, 1998: Hydrography of the upper Arctic Ocean measured from the nuclear submarine U. S. S. *Pargo. Deep Sea Res. Part I-Oceanogr. Res. Pap.*, **45**, 15–38.

Ohlmann, J. C., 2003: Ocean radiant heating in climate models. *J. Climate*, **16**, 1337–1351.

Paulson, C. A., and J. J. Simpson, 1977: Irradiance measurements in the upper ocean. *J. Phys. Oceanogr.*, **7**, 952–956.

Rayner, N. A., D. E. Parker, E. B. Horton, et al., 2003: Global analyses of sea surface temperature, sea ice, and night marine air temperature since the late nineteenth century. *J. Geophys. Res.*, **108**, doi: 10.1029/2002JD002670.

Redi, M. H., 1982: Oceanic isopycnal mixing by coordinate rotation. *J. Phys. Oceanogr.*, **12**, 1154–1158.

Smith, T. M., R. W. Reynolds, T. C. Peterson, et al., 2008: Improvements NOAA's historical merged land–ocean surface temperature analysis (1880–2006). *J. Climate*, **21**, 2283–2296.

St. Laurent, L. C., H. L. Simmons, and S. R. Jayne, 2002: Estimating tidally driven mixing in the deep ocean. *Geophys. Res. Lett.*, **29**, 21-1–21-4, doi: 10.1029/2002GL015633.

Steele, M., R. Morley, and W. Ermold, 2001: PHC: A global ocean hydrography with a high-quality Arctic Ocean. *J. Climate*, **14**, 2079–2087.

Taylor, K. E., R. J. Stouffer, and G. A. Meehl, 2012: An overview of CMIP5 and the experiment design. *Bull. Amer. Meteor. Soc.*, **93**, 485–498, doi: 10.1175/BAMS-D-11-00094.1.

Wang, C. Z., L. P. Zhang, S.-K. Lee, et al., 2014: A global perspective on CMIP5 climate model biases. *Nat. Clim. Change*, **4**, 201–205.

Xie, P. P., and P. A. Arkin, 1997: Global precipitation: A 17-yr monthly analysis based on gauge observations, satellite estimates, and numerical model outputs. *Bull. Amer. Meteor. Soc.*, **78**, 2539–2558.

Xue, Y., T. M. Smith, and R. W. Reynolds, 2003: Interdecadal changes of 30-yr SST normals during 1871–2000. *J. Climate*, **16**, 1601–1612.

Yu Yongqiang, Yu Rucong, Zhang Xuehong, et al., 2002: A flexible global coupled climate model. *Adv. Atmos. Sci.*, **19**, 169–190.

Zhang, X. H., W. Y. Lin, and M. H. Zhang, 2007: Toward understanding the double intertropical convergence zone pathology in coupled ocean-atmosphere general circulation models. *J. Geophys. Res.*, **112**, D12102, doi: 10.1029/2006JD007878.

Zhou Tianjun, Chen Xiaolong, Dong Lu, et al., 2014: Chinese contribution to CMIP5: An overview of five Chinese models' performances. *J. Meteor. Res.*, **28**, 481–509.